Chinese Journal of Chemical Engineering 69 (2024) 112–121

Contents lists available at ScienceDirect

Chinese Journal of Chemical Engineering

journal homepage: www.elsevier.com/locate/CJChE

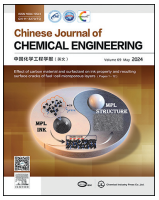

Full Length Article

Removal of rubidium from brine by an integrated film of sulfonated polysulfone/graphene/potassium copper ferricyanide

Huanxi Xu [1], Peihua Lin [1], Pei-Jun Liu [1], Hai-Gang Liu [2], Hui-Bin Guo [2], Chao-Xiang Wu [2], Ming Fang [1], Xu Zhang [1], Guan-Ping Jin [1,*]

[1] *Anhui Province Engineering Research Center of Flexible and Intelligent Materials, School of Chemistry and Chemical Engineering, Hefei University of Technology, Hefei 230009, China*
[2] *Chemical Design and Research Institute Co., LTD of Qinghai Province, Qinghai Engineering and Technology Research Center of Fine Chemical, Xining 810008, China*

ARTICLE INFO

Article history:
Received 12 April 2023
Received in revised form
16 November 2023
Accepted 28 November 2023
Available online 1 March 2024

Keywords:
Rubidium extraction
Potassium copper ferricyanide
Sulfonated polysulfone
Graphene oxide
Adsorption

ABSTRACT

A novel integrated film of sulfonated polysulfone/graphene/potassium copper ferricyanide (KCuFC/SPSG) was used for selectively extracting rubidium ion (Rb^+) from brine. To form KCuFC/SPSG, the precursor film of sulfonated polysulfone/graphene (SPSG) was synthesized by phase conversion process, which was alternately immersed in 0.1 $mol \cdot L^{-1}$ $CuSO_4/K_4[Fe(CN)_6]$ by *in-situ* adsorption coupled co-precipitation method. Various data such as nuclear magnetic resonance spectrometer, Fourier transform infrared spectroscope, X-ray photoelectron spectroscope, X-ray diffraction, scanning electron microscope, and energy dispersive spectroscopy all verified that abundant KCuFC were uniformly located on the film. The resulting KCuFC/SPSG was used in film separation system. As the solution was fed into the system, the Rb^+ could be selectively adsorption by KCuFC/SPSG. After the saturation adsorption, 0.5 $mol \cdot L^{-1}$ NH_4Cl/HCl was fed into the film cell, Rb^+ could be quickly desorbed by ion-exchange between Rb^+ and NH_4^+ in the lattice of KCuFC. The purpose of separating and recovering Rb^+ from the brine can be achieved after the repeated operation. The effects of pH, adsorption time, and interferential ions on the adsorption capacity of Rb^+ were investigated by batch experiments. The adsorption behavior fits the pseudo-second order kinetic process, while KCuFC has a higher adsorption capacity (Langmuir maximum sorption 165.4 $mg \cdot g^{-1}$). In addition, KCuFC/SPSG shows excellent selectivity for Rb^+ even in complex brine systems. KCuFC/SPSG could maintain 93.5% extraction efficiency after five adsorption/desorption cycles.

1. Introduction

Rubidium (Rb) is a rare metal with unique photoelectric properties, which is widely used in high-technology domain, include specialty glass [1], laser cooling [2], medicine [3], photomultiplier tube [4], and atomic clock [5]. Rubidium is growing in demand as an important industrial raw material. Rubidium is commonly found in granite pegmatites, seawater, and salt lakes [6–8]. The extraction of rubidium from water resources is increasingly favored due to depletion of mineral resources. Among various methods have been reported on the separation, such as precipitation [9,10], extraction [11], and adsorption [12], the adsorption method has become a popular research direction [13–15]. Hexacyanoferrates (KMFC) are promising adsorbents with good selectivity and high adsorption capacity [16,17]. The cavity size of KMFC lattice is similar to the unhydrated radius of Rb^+ (radii of hydration and unhydrated radii of the different ions are shown in Table 1) [16]. During the adsorption process, Rb^+ could enter the lattice and replace the K^+ in KMFC [18–20]. Experiments comparing the rubidium removal effects of potassium copper ferricyanide (KCoFC) and ammonium molybdophosphate (AMP) showed that KCoFC has a higher capacity to adsorb Rb^+ [12]. Moreover, the researchers immobilized KNiFC into biopolymer foam and applied it to the adsorption of Cs^+ [21]. In comparison with KNiFC and KCoFC, KCuFC shows unprecedented kinetics and reversibility. Study shows that KCuFC, KCoFC and KNiFC have different adsorption capacities for Rb^+ under the same conditions. The KCuFC has a higher adsorption capacity and more milder desorption conditions compared to KCoFC and KNiFC.

* Corresponding author.
E-mail address: jgp@hfut.edu.cn (G.-P. Jin).

https://doi.org/10.1016/j.cjche.2023.11.028
1004-9541/

Table 1
Hydration and unhydration radius of different ions [16]

Metal ion	Hydrated ionic radius/nm	Unhydrated ionic radius/nm
Li	0.340–0.470	0.060
Na	0.276–0.360	0.095
K	0.232–0.331	0.133
Rb	0.228	0.148
Cs	0.226–0.228	0.168
Mg	0.300–0.470	0.066

Desorption of Rb^+ from KCoFC or KNiFC using KCl has been reported in Refs. [21,22]. This type of desorption, however, introduces new metal ions into the purification solution. Moreover, the researcher used a simple method of switching electrode potentials for desorption [20]. Different from the desorption methods of KCoFC and KNiFC, Rb^+ is easily desorbed from KCuFC in NH_4Cl.

The particle size of KCuFC is small; therefore, it is difficult to separate it from the solution. To overcome this problem, polymer materials are usually used to load KCuFC particles [23]. Membrane (or film) separation technology has been widely used to extract trace metals from seawater or salt lakes due to its low energy consumption, good separation effect, and simple process [24,25]. Recently, the separation of Rb^+ (Cs^+) using membrane (or film) materials as carriers of adsorbents has become increasingly popular. For instance, adsorbents were immobilized onto polyvinylidene fluoride, polyvinyl chloride, polyvinyl pyrrolidone membranes, or cellulose nanocrystallines film, respectively [26–28]. Sulfonated polysulfone has excellent physical and chemical properties, such as good mechanical strength, resistance to oxidation, acids and bases. Sulfonated polysulfone composite membranes are mainly the application of proton exchange membranes for fuel cells [29,30]. For the past few years, studies gradually progressed to desalination [31]. Notably, ammonium phosphomolybdate wrapped in polysulfone membranes was applied for the recovery of Rb^+ [32]. Nevertheless, this method results in a significant decrease in adsorption capacity, as the membrane obscures some of the adsorption sites. Therefore, the spatial structure of the film is improved to facilitate adsorption and desorption.

Previous studies have shown that KCuFC nanoparticles synthesized by co-precipitation are very susceptible to agglomeration. Graphene oxide (GO) with unique physical and chemical properties (including excellent lamellar sheet structure and abundant oxygen-containing groups: −COOH, C═O, and −OH) is often utilized for adsorption of heavy metal ions [33,34]. First, GO is used to immobilize Cu^{2+}, following which Cu^{2+} is further converted into KCuFC. The synthesized KCuFC particles by this method are uniformly distributed, which facilitates the adsorption and desorption process.

In this work, films were co-cast using GO and sulfonated polysulfone. A three-dimensional (3D) porous film of sulfonated polysulfone/graphene (SPSG) was then made using phase inversion technique. Then, the film was alternately immersed in $CuSO_4$ and $K_4[Fe(CN)_6]$ solution to co-precipitation and uniformly form KCuFC nanoparticles (KCuFC/SPSG). Here, GO not only improves the space structure of film but also provides a large number of landing sites for KCuFC. In this work, the use of KCuFC/SPSG films to separate rubidium in solution was studied in detail.

2. Experimental

2.1. Material and chemicals

Polysulfone (PS), chlorosulfonic acid (HSO_3Cl, 99.9%), chlorotrimethylsilane ($(CH_3)_3SiCl$, 99.9%), chloroform and *N,N*-dimethylacetamide (DMAc) were acquired from Aladdin Biochemical Technology Co., Ltd. (Shanghai, China). Methyl alcohol (CH_3OH), sodium methanolate (CH_3ONa), copper sulfate pentahydrate ($CuSO_4·5H_2O$), potassium hexacyanoferrate ($K_4[Fe(CN)_6]$), lithium chloride (LiCl), sodium chloride (NaCl), magnesium chloride ($MgCl_2$), potassium chloride (KCl), and rubidium chloride (RbCl) were all purchased from Sinopharm Chemical Reagent Co., Ltd (Shanghai, China).

2.2. Characterization

The functional groups on KCuFC/SPSG were tested by Fourier transform infrared spectroscope (FTIR, IR 200, Nicolet, USA) and nuclear magnetic resonance spectrometer (NMR, JNM-ECZ400S, JEOL, Japan). The morphology and composition of the KCuFC/SPSG were analyzed using scanning electron microscope and energy dispersive spectroscopy (SEM, SU8020, Hitachi, Japan). The crystal data were collected using X-ray diffraction (XRD, X-Pert PRO MPD, PANalytical, Netherlands). The variations in the chemical composition of KCuFC/SPSG surface were offered during the extraction process of Rb^+ by X-ray photoelectron spectroscope (XPS, ESCALAB250Xi, Thermo, USA). The metal ion content was measured by inductively coupled plasma mass spectrometry (ICP-MS, Agilent 7900, USA).

2.3. Preparation of KCuFC/SPSG film

A schematic diagram of the synthesis and adsorption process of KCuFC/SPSG films is shown in Fig. 1.

2.3.1. Sulfonation of polysulfone (PS)

The PS was sulfonated according to Refs. [29]. The 10 g PS was dissolved in dried chloroform under stirring, 4.8 g $(CH_3)_3SiCl$ in chloroform was slowly added, then, a solution containing chlorosulfonic acid in chloroform was added drop by drop with 1 h. The obtained solution was vigorously stirred at 35 °C for 12 h. After that, sodium methanolate solution was poured into the mixture under stirring, sulfonated polysulfone (SPS) could be precipitated. SPS was washed with deionized water (DI water), and vacuum dried at 60 °C. The molar ratio between the PS and sulfonation agent were 1:2.

2.3.2. Graphene oxide and sulfonated polysulfone films (SPSG)

Film was prepared by the phase inversion technique. 50 mg GO was added to 20 ml DMAc with 2 h ultrasonication, then, 10 g SPS was put in. The casting solution was poured on a glass plate, and a film applicator was used to preparing film. After that, the film was immediately immersed into water coagulation bath of 25 °C for phase separation [15]. Obtained film named SPSG.

2.3.3. Sulfonated polysulfone/GO/potassium copper ferricyanide film (KCuFC/SPSG)

The SPSG film was put in 0.1 $mol·L^{-1}$ $CuSO_4$ with 12 h to adsorb Cu^{2+} and washed repeatedly with DI water. After that, the film was immerged in 0.1 $mol·L^{-1}$ $K_4[Fe(CN)_6]$ for 12 h, and washed again. The film obtained named KCuFC/SPSG.

2.4. Separation of Rb^+ using KCuFC/SPSG

2.4.1. Adsorption kinetics

The adsorption kinetics of Rb^+ on KCuFC/SPSG was investigated by dynamic adsorption method at room temperature. KCuFC/SPSG was fixed in a homemade film cell. 200 ml of Rb^+ (20 $mg·L^{-1}$, pH = 7.0 ± 0.5) was placed in a beaker. The solution was circulated through

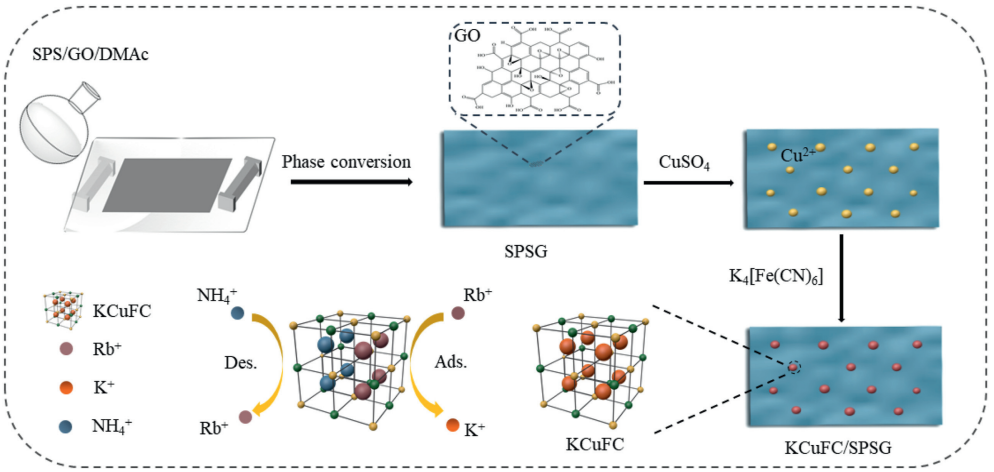

Fig. 1. The schematic diagram of the synthesis and adsorption/desorption process of KCuFC/SPSG.

the film cell by a peristaltic pump for 6 h. The adsorption capacity (Q_e, mg·g^{-1}) was calculated as [17].

$$Q_e = \frac{(C_0 - C_e) \times V}{m} \quad (1)$$

where C_0 is initial concentration of Rb^+ (mg·L^{-1}); C_e is equilibrium concentration of Rb^+ (mg·L^{-1}); V is volume of the solution (L), and m is the mass of KCuFC on KCuFC/SPSG (g).

2.4.2. Desorption of Rb^+ from the KCuFC/SPSG

After the adsorption equilibrium of Rb^+ on the KCuFC/SPSG, the desorption of Rb^+ was performed in 200 ml and 0.5 mol·L^{-1} NH_4Cl/HCl with different time, and the rate of peristaltic pump is rate of 50 ml·min^{-1}.

3. Results and Discussion

3.1. Characterization of KCuFC/SPSG

3.1.1. ^1H NMR

The comprise of PS and SPS were confirmed by ^1H NMR in Fig. 2. It can be seen from Fig. 2 that the chemical shifts at δ 7.7 was attributed to the proton adjacent to the new pendent sodium sulfonate [30].

3.1.2. FT-IR

To solidify the above observation, the SPSG (a), KCuFC (b), KCuFC/SPSG before (c) and after adsorption (d) were characterized by FT-IR in Fig. 3. In curve (a), absorption bands were associated

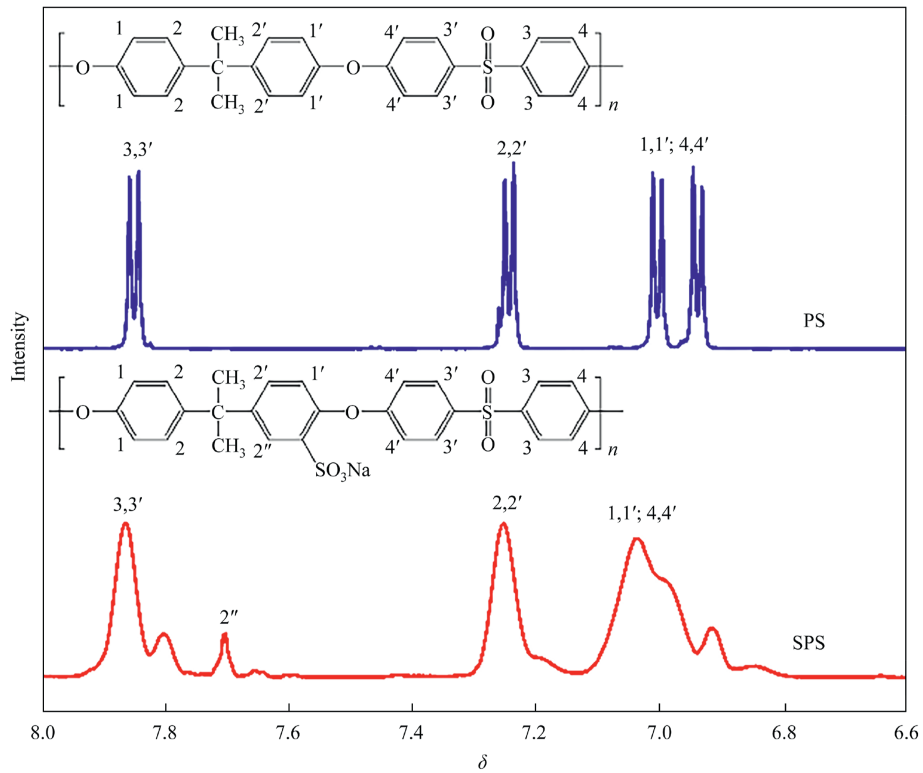

Fig. 2. ^1H NMR spectra of PS and SPS.

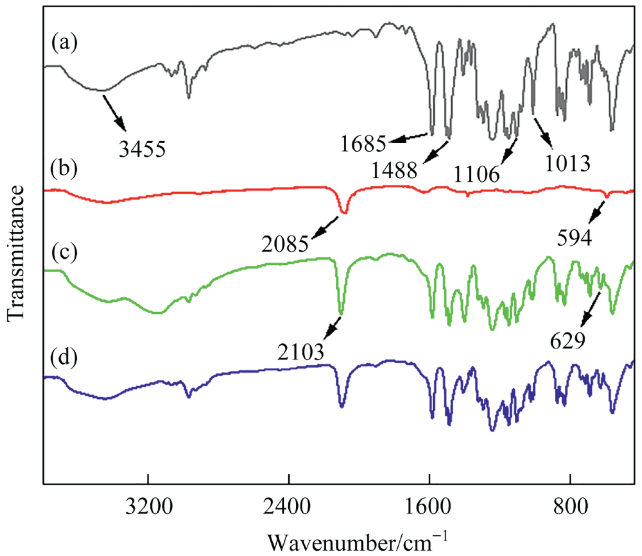

Fig. 3. FTIR spectra of SPSG (a), KCuFC (b), KCuFC/SPSG before (c) and after adsorption (d).

with O═S═O stretching vibration (1106 cm^{-1}) of sulfonic acid group, S═O stretching vibrations (1013 cm^{-1}) [29]. The −OH absorption peak was located at 3450 cm^{-1}, and the −RCOOH and C═C absorption peaks were related to 1685 and 1488 cm^{-1}. In curve (b), KCuFC was shown two topical peaks at 2085 and 594 cm^{-1}, which were the absorption peak of −CN and Fe−CN [35]. It is readily seen that all the peaks in curves (a) and (b) show in curve (c) too, suggesting the formation of KCuFC/SPSG. Further, the peaks in KCuFC/SPSG still could be observed same peaks at 2103 and 629 cm^{-1} after the once of Rb^+ adsorption/desorption process, belonging to −CN and Fe−CN, implying a stability for the structure.

3.1.3. SEM

Fig. 4 shows physical view (a) of SPSG (left) and KCuFC/SPSG (right), SEM images of KCuFC/SPSG (b, d) and SPSG (c). SPSG is a milky white film (a, left), while KCuFC/SPSG is brick red film (a, right), suggesting uniform load of KCuFC on SPSG. The surface of SPSG shows porous structure (c, right), the cross-sectional view appears a 3D porous structure with diameters of 5–12 μm, and the wall is clear (c, left). It is predicable that the present stereoscopic and multihole film will facilitate the loading of KCuFC and mass transfer. It is interesting for the images of KCuFC/SPSG (b, d), plenty of KCuFC nano-particles could be uniformly dispersed at the outside and inside of KCuFC/SPSG, and the wall is very rough compared that of only SPSG, suggesting the formation. It is noticeably that the 3D porous film structure still could be readily seen, which is beneficial for the separation of Rb^+.

3.1.4. XRD

XRD data of KCuFC/SPSG before (a) and after (b) adsorption Rb^+, desorption Rb^+ (c), and SPSG (d) are shown in Fig. 5. In curve (a), there are five sharp peaks at 17.8°, 25.2°, 36.0°, 40.2° and 44.3°, which are diffractions from the (2 0 0), (2 2 0), (4 0 0), (4 2 0) and (4 2 2) crystal planes of KCuFC, respectively [35]. All the peaks still could be seen in curve (b) and (c), indicating that the structure of KCuFC is stable during adsorption/desorption on the film. The reason is probably related that the GO on the film gave many attachment sites for KCuFC/SPSG, which is consistent with the result in Fig. 2. Moreover, two sharper characteristic peaks of NaCl at 31.8° (2 0 0) and 45.5° (2 2 0) could be seen in SPSG film [36], which disappeared after full cleaning (no show). Because CH_3ONa

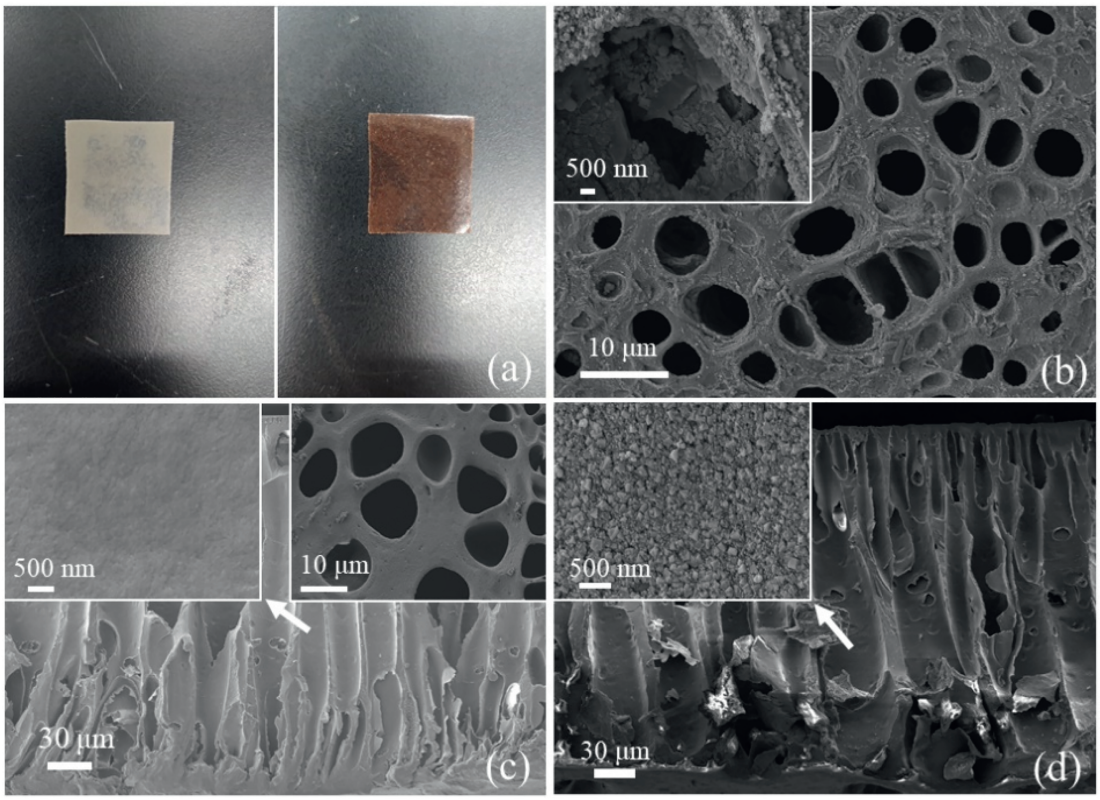

Fig. 4. Physical view (a) of SPSG (left) and KCuFC/SPSG (right), SEM images of KCuFC/SPSG (b, d) and SPSG (c).

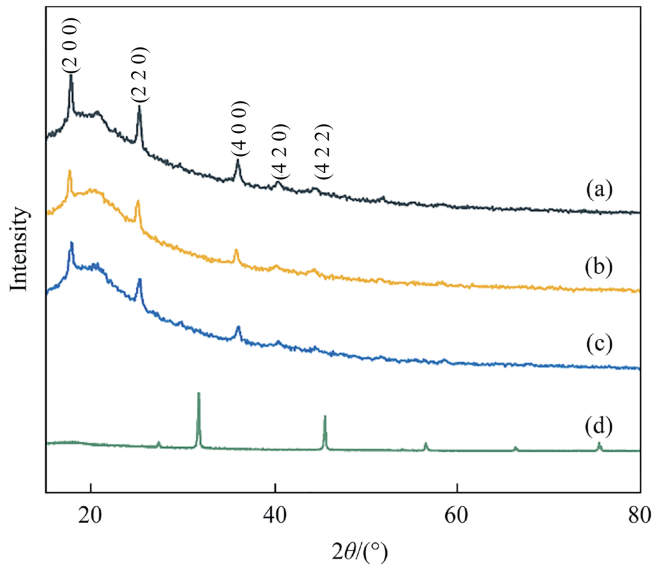

Fig. 5. XRD patterns of KCuFC/SPSG before (a) and after (b) adsorption Rb^+, after desorption Rb^+ (c), and SPSG (d).

and $(CH_3)_3SiCl$ were used in the synthesis of SPS, which resulted residual of NaCl. The average particle size of KCuFC nanoparticles was calculated using Debye–Scherrer equation [35]:

$$D = \frac{k\lambda}{\beta \cdot \cos\theta} \tag{2}$$

where D is the crystal size of KCuFC (nm), the k is Scherrer constant (0.95), the λ is wavelength of X-rays, the β is half-peak width of the diffraction peak, and the θ is Bragg diffraction angle. The three major diffraction peak date (17.8°, 25.2° and 36.0°) are calculated by the above equation, and the KCuFC crystal particles with a size of 22.5 nm.

To further confirm the elemental composition, the elemental distribution of KCuFC/SPSG film was analyzed by EDS elemental mapping. Fig. 6 shows the existences of main elements such as C, O, Fe, and Cu in the film. This is a good indication of the successful grafting of KCuFC onto the film. It is noticeable that much Rb could be observed after the adsorption (left) using KCuFC/SPSG, there is a little Rb after the desorption (right). These illustrates the present KCuFC/SPSG film could be used the separation of Rb.

3.1.5. XPS

As shown in Fig. 7(a), XPS full survey spectra appears spectrum of Cu 2p, Fe 2p, C 1s and O 1s at KCuFC/SPSG film. The peaks at 935.9 and 933.2 eV are belonged to Cu $2p_{3/2}$, and at 955.8 eV are related to Cu $2p_{1/2}$ in Fig. 7(b). The peaks with Fe $2p_{3/2}$ and Fe $2p_{1/2}$ can be observed at 708.9 and 721.6 eV in Fig. 7(c). As seen in Fig. 7(d), the image of C 1s shows that the peaks at 284.77–286.27 eV are associated with the C–C and C–O in the material. The presence of C–O and C=O within this material is confirmed by the peaks of 531.72 and 533.32 eV in Fig. 7(e) [37,38]. All above the results prove the formation of KCuFC/SPSG film. In Fig. 7(f), before the adsorption, there is not peak of Rb at KCuFC/SPSG film. After the adsorption, two dominated peaks of Rb $3d_{5/2}$ (110.48 eV) and Rb $3d_{3/2}$ (111.93 eV) could be observed [39]. Therefore, the present KCuFC/SPSG film is promising for the recovery of Rb^+.

3.2. Separation experiments

3.2.1. Effect of pH on Rb adsorption

The pH is an important factor in many adsorption systems. Here, pH of the solution was adjusted using HCl and NaOH with a range of 4–9. As shown in Fig. 8, the adsorption capacity of KCuFC/SPSG toward Rb^+ appears a parabolic trend at pH 4–9. At lower pH, there

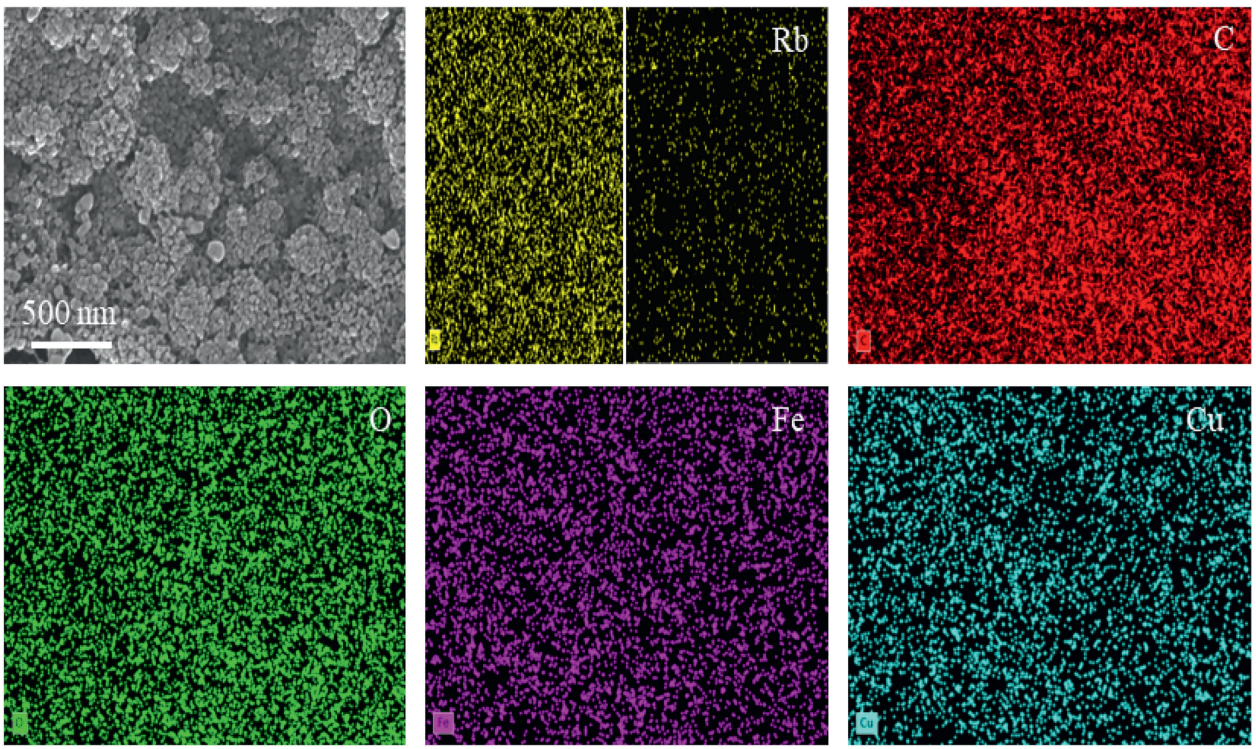

Fig. 6. EDS of Rb after adsorption (left) and after desorption; C, O, Fe and Cu at KCuFC/SPSG.

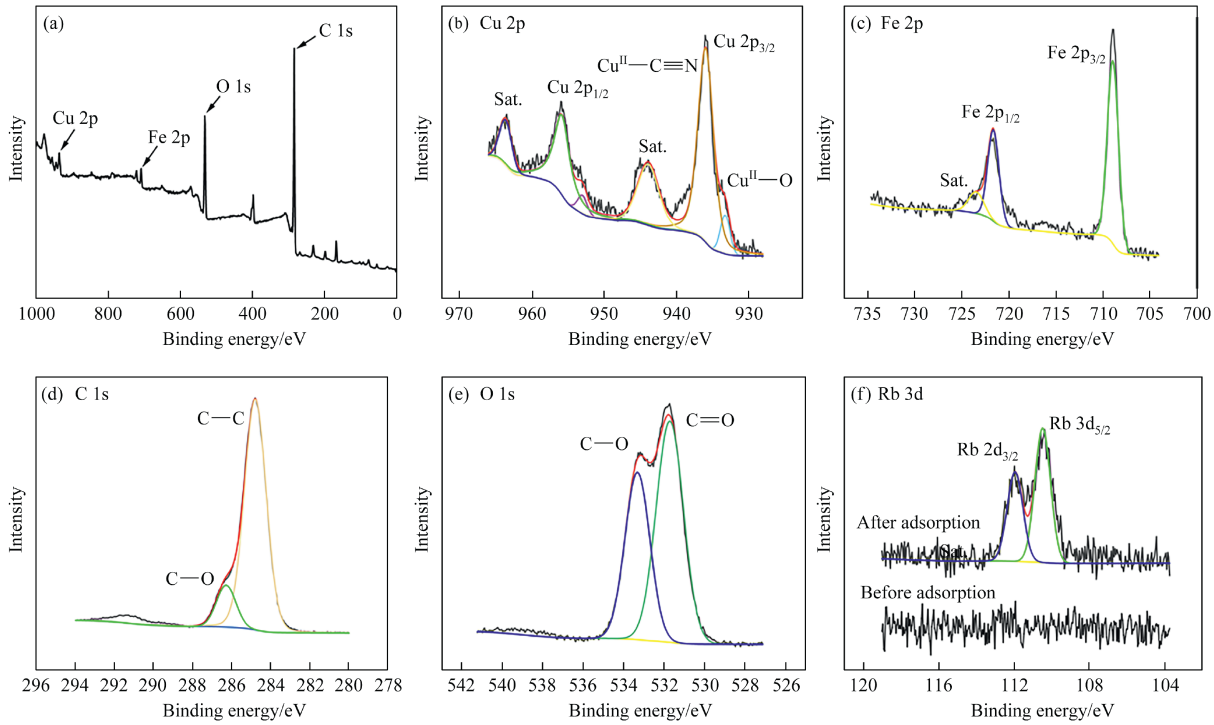

Fig. 7. XPS spectra of KCuFC/SPSG (a), Cu 2p (b), Fe 2p (c), C 1s (d), O 1s (e) and Rb 3d (f).

may be adsorption competition between H^+ and Rb^+ in highly acidic solution. The suitable adsorption could be performed at a range of pH 6–8, and the maximum adsorption capacity is 73.7 $mg \cdot g^{-1}$ at pH 7.0. The increased [OH^-] probably facilitate the adsorption of Rb^+ at KCuFC/SPSG by electrostatic adsorption. The higher pH is not allowed because the lattice size of KCuFC could be destroyed by higher concentration of OH^- [38].

3.2.2. Adsorption kinetics

In Fig. 9(a), the adsorption capacity of KCuFC/SPSG toward Rb^+ was investigated depending on time in 5, 10 and 20 $mg \cdot L^{-1}$ of Rb^+ with pH 7. At concentration of 5 $mg \cdot L^{-1}$, quickly reaches adsorption equilibrium in nearly first 0.5 h with adsorption capacity of 36.5 $mg \cdot L^{-1}$, there is not obvious increase with the delay of time, which is probably dominant by the outside KCuFC in the film. The same could be observed at concentrations of 10 and 20 $mg \cdot L^{-1}$ for the first 0.5 h, with a rapid increase in adsorption capacity with increasing contact time. The adsorption capacity can reach 78.6% of the maximum adsorption capacity in the first 0.5 h. The adsorption capacity is continuingly increased with the increasing time, while the adsorption rate gradually slows down, and reaching stability at 3 h. After 3 h, the adsorption capacity is essentially stable, suggesting adsorption equilibrium. The adsorption of Rb^+ can be divided into two stages. The first stage is the rapid adsorption stage, where Rb^+ was rapidly adsorbed on the surface of KCuFC due to the presence of abundant adsorption sites, and then Rb^+ was transported into the inside through the pores on the surface of the film. Meanwhile, the higher concentration of Rb^+ in the solution provided a stronger driving force for mass transfer for adsorption. The second stage is the slow adsorption stage, in which the mass transfer driving force decreases with the gradually reduced concentration of Rb^+ in the solution.

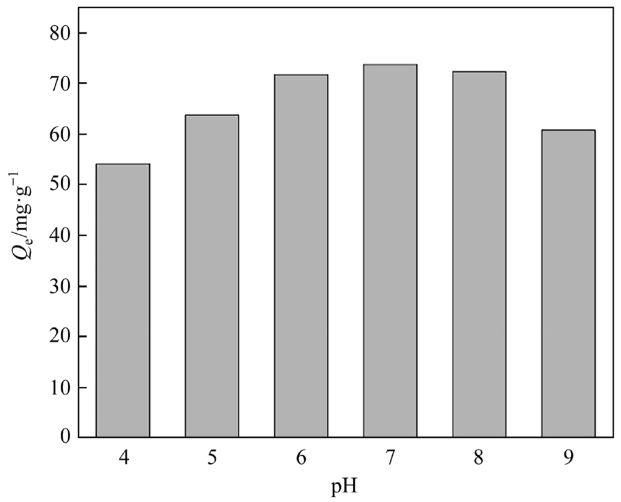

Fig. 8. Adsorption capacity at different pH.

To further investigate the capture behavior of Rb^+ on KCuFC/SPSG film, two adsorption kinetic models were adopted to analyze the adsorption process of Rb^+. The calculation methods of pseudo-first-order and pseudo-second-order model are shown in Eqs. (3) and (4) [27].

Pseudo-first-order:

$$Q_t = Q_e\left(1 - \exp^{-k_1 t}\right) \tag{3}$$

Pseudo-second-order:

$$Q_t = k_2 Q_e^2 t/(1 + k_2 Q_e t) \tag{4}$$

where Q_t ($mg \cdot g^{-1}$) and Q_e ($mg \cdot g^{-1}$) are the equilibrium adsorption amount of Rb^+ by KCuFC/SPSG film and time t (h), respectively. The rate constants k_1 (h^{-1}) correspond to the pseudo-first-order

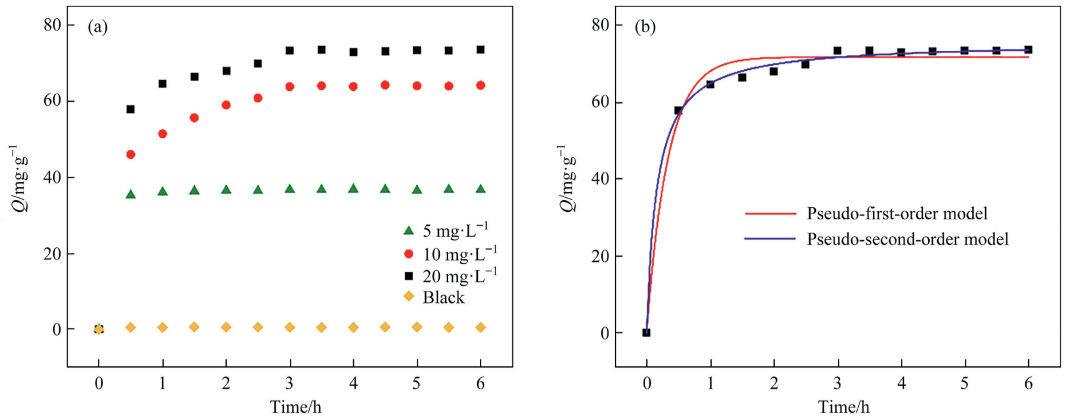

Fig. 9. Adsorption capacity depending on Rb concentrations (a) and kinetics plot for the adsorption of Rb^+ on KCuFC/SPSG (b). C_0 = 20 mg·L^{-1}, pH 7.

parameter, and k_2 (mg·g^{-1}·h^{-1}) is the adsorption rate constant of pseudo-second-order model parameters. The parameters are summarized in Table 2. R^2 is the correlation coefficient, if R^2 is closer to 1, the stronger the predictive power of the model. It can be seen that the R^2 of the pseudo-second-order kinetic model for KCuFC/SPSG film adsorption of Rb^+ is much closer to 1. This suggests that the kinetics of the type of Rb^+ adsorption on the KCuFC/SPSG film was more compatible with chemisorption [27].

3.2.3. Adsorption isotherm

To further study the adsorption behavior of KCuFC, adsorption experiments were carried out at room temperature and 5–200 mg·L^{-1} of Rb^+. As indicated in the figure, the adsorption capacity of KCuFC increases with increasing concentration of the solution. The adsorption capacity of KCuFC increased significantly at lower concentrations of 5–100 mg·L^{-1} of solution, and relatively, the adsorption capacity of KCuFC increases slowly in high concentrations of Rb^+ solutions. It is attributed to the fact that higher concentrations provide higher mass transfer kinetics, and the increase in the adsorption capacity of KCuFC slows down when its recognition sites become saturated.

Langmuir model:

$$Q_e = \frac{Q_m K_L C_e}{1 + K_L C_e} \tag{5}$$

Freundlich model:

$$Q_e = K_F C_e^{1/n} \tag{6}$$

where K_L and K_F are the Langmuir and Freundlich model constants, respectively, Q_m is the theoretical adsorption capacity of KCuFC/SPSG film, $1/n$ represents the measure of exchange intensity or surface affinity of the solute [27].

The Langmuir and Freundlich models have been used to describe the adsorption data and the fitted curves and related parameters are shown in Fig. 10 and Table 3. According to the data in Table 3, the correlation coefficient of Langmuir isotherm (R^2 = 0.9831) is larger than that of Freundlich isotherm (R^2 = 0.9691), representing that the Langmuir adsorption model is more suitable for describing the adsorption of Rb^+ by KCuFC/SPSG film [22]. It means that by monolayer adsorption Rb^+ is homogeneously immobilized on the surface or holes of film. Benefiting from the unique synthesis method of KCuFC, the time to reach adsorption equilibrium of KCuFC is shorter, meanwhile the theoretical adsorption capacity (Q_{max} = 165.4 mg·g^{-1}) of KCuFC is higher as compared to the previously reported in Ref. [7].

Table 2
Linear fitting constants of adsorption kinetic models for KCuFC/SPSG film

Initial C_{Rb}^+/mg·L^{-1}	Q_e	Pseudo-first-order model			Pseud-second-order model		
		k_1	$Q_{e1,\,cal}$	R^2	k_2	$Q_{e2,\,cal}$	R^2
20	73.7	2.96	71.7	0.9833	0.59	75.6	0.9969

3.2.4. Adsorption selectivity

Since Rb^+ is usually coexists with various ions including Na^+, K^+, Li^+, Mg^{2+} in real brine. The adsorption of Rb^+ on KCuFC/SPSG in the presence of interfering ions was investigated in a mixed solution including Na^+, K^+, Li^+, Mg^{2+} and Rb^+ with same concentration of 20 mg·L^{-1} (pH 7, 3 h and room temperature). After the adsorption, the residual solution was detected by ICP-MS. The concentration difference between original and residual concentration is the adsorption capacity. The selective separation of Rb^+ was calculated by following equation:

$$\alpha_M^{Rb} = \frac{C_M\, Q_{Rb}}{C_{Rb}\, Q_M} \tag{5}$$

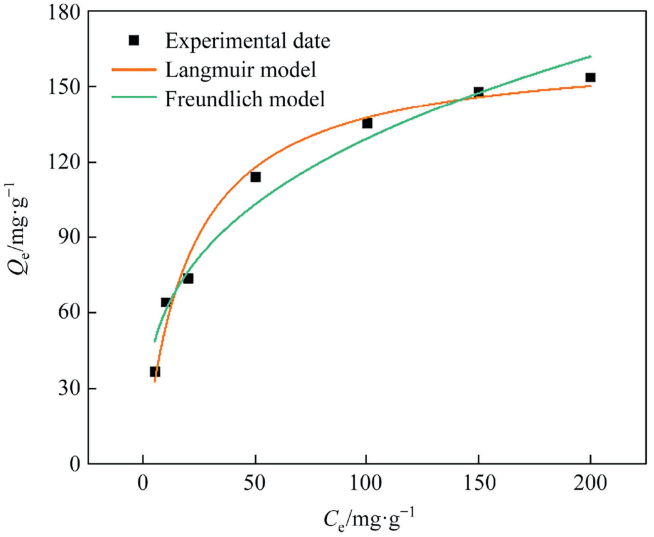

Fig. 10. Adsorption isotherm plots of Rb^+ on KCuFC/SPSG film.

Table 3
Adsorption models and parameters for Rb^+ adsorption on KCuFC/SPSG film

Langmuir model			Freundlich model		
Q_{max}/mg·g^{-1}	K_L/L·mg^{-1}	R^2	n	K_F/(mg·g^{-1}) (L·mg^{-1})$^{1/n}$	R^2
165.4	20.3	0.9831	3.07	28.5	0.9691

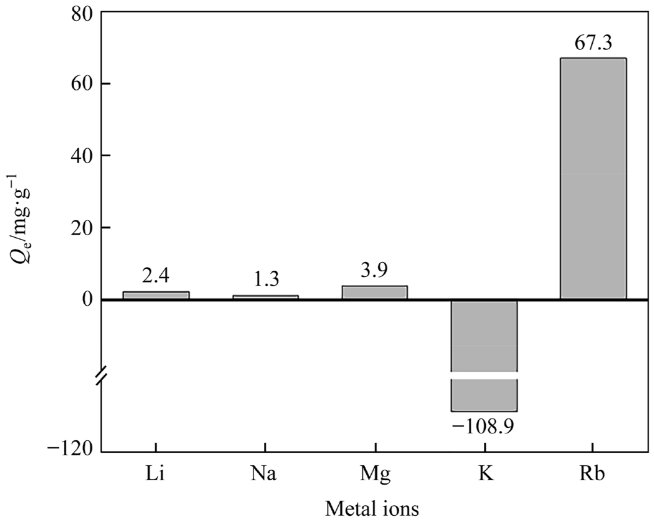

Fig. 11. Adsorption capacity of Rb^+ on KCuFC/SPSG in coexist of competing ions.

where C_M and C_{Rb} are the concentrations of competing ions and Rb^+ at adsorption equilibrium, respectively. Q_M and Q_{Rb} are the adsorption capacities of competing ions and Rb^+, respectively. The separation coefficients of Li^+, Na^+ and Mg^{2+} were calculated as 54.9, 88.1 and 33.3, respectively. Fig. 11 also shows the promising separation, it is noticeable that the higher concentrations of K^+ in the solution is due to the replacement of K^+ on KCuFC/SPSG by Rb^+ during the adsorption process, and the possible presence of $K_4[Fe(CN)_6]$ remained by synthesis of KCuFC/SPSG. The reaction equation is as follows:

$$K_2Cu[Fe(CN)_6] + 2Rb^+ \rightarrow Rb_2Cu[Fe(CN)_6] + 2K^+$$

The good selectivity of KCuFC/SPSG to Rb^+ separation could be explained by the radius of ions and the cavity size of KCuFC. Since smaller the hydrated radius of ions, the easier it is for the ion to approach surface of adsorbent, the hydration ionic radii: Cs^+ (0.226–0.228 nm), Rb^+ (0.228 nm), K^+ (0.232–0.331 nm) and NH_4^+ (0.331 nm) [16], and the unhydrated ionic radii: Rb^+ (0.148 nm), NH_4^+(0.148 nm) and K^+ (0.133 nm). The cavity size of KCuFC lattice is similar to the unhydrated radius of Rb^+, thus making Rb^+ easy enter the lattice replace K^+, and Rb^+ on KCuFC/SPSG could be exchanged by NH_4^+ too.

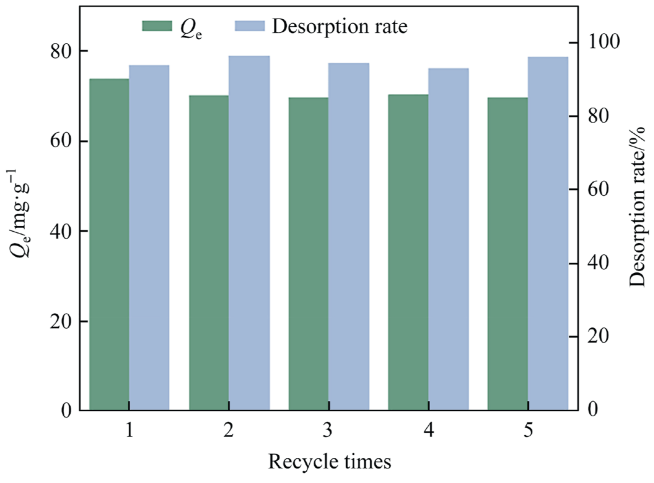

Fig. 12. Separation effect of KCuFC/SPSG to Rb^+ in the continuous process of 1–5.

Table 4
Comprise of brine (mg·L^{-1})

	Li^+	Na^+	Mg^{2+}	K^+	Rb^+	Cs^+
Brine	5.3	510.8	7584.0	1979.0	7.9	0.18
Purifying	0.003	1.7	61.4	40.6	3.9	0.05

Table 5
Ratio of Rb^+ and the other ions in brine and purification solution

	Li^+/Rb^+	Na^+/Rb^+	Mg^{2+}/Rb^+	K^+/Rb^+	Cs^+/Rb^+
Brine	0.7	64.1	951.9	248.3	0.02
Purification solution	0.001	0.4	15.8	10.5	0.01

3.2.5. Regeneration

After the adsorption of Rb^+ using KCuFC/SPSG, prior to the desorption step, the surface of KCuFC/SPSG (Rb^+) was washed with deionized water to eliminate contamination from other salts. Then, KCuFC/SPSG (Rb^+) undergone desorption in film cell for 3 h using 200 ml, 0.5 mol·L^{-1} of NH_4Cl/HCl. The adsorption/desorption step was repeated 5 times to study the recyclability of KCuFC/SPSG. As shown in Fig. 12, the adsorption capacities of first and fifth were 73.7 and 69.6 mg·g^{-1} with only reduce of 5.6%. Moreover, the every time desorption rate is more than 90%. Thus, the present KCuFC/SPSG film shows excellent regeneration ability.

3.3. Application in brine

Above facts confirmed that KCuFC/SPSG film has good adsorption and selectivity properties. It is important to investigate the separation of Rb^+ using KCuFC/SPSG film in brine environment. In the same conditions including pH 7, adsorption of 3 h, desorption of 3 h and pump rate of 50 ml·min^{-1} at room temperature. 200 ml of brine was circulated through the film cell. After the adsorption, cleaning film cell with DI, 200 ml, 0.5 mol·L^{-1} NH_4Cl/HCl were pumped into the film cell to desorb Rb^+, then, resorption solution of Rb^+ could be obtained. The concentration of ions was detected using ICP-MS. The resorption solution was singed as Rb^+ purifying solution. Table 4 shows the comprise of both brine and purifying solution. In comparison with that of the brine, 52.5% of Rb^+ in the brine (7.9 mg·L^{-1}) could be recovered in the purification solution (3.9 mg·L^{-1}), in which the level of Li^+ (0.003 mg·L^{-1}) and Na^+ (1.7 mg·L^{-1}) are obviously lesser, suggesting low interferes. The higher concentrations of Mg^{2+} (61.4 mg·L^{-1}) contained in the purification solution may be due to the high levels of both ions in the brine, which remained on the film surface during the adsorption. Since there is competition adsorption between K^+ and Rb^+, which results the higher level of K^+ (40.6 mg·L^{-1}) in the purification solution. 28% of Cs^+ (0.05 mg·L^{-1}) could be recovered due to their

similar ionic radius and which are both well adsorbed by KCuFC. On the other hand, owing to the interference of coexistence ions, and weaker mass transfer dynamic resulted by the low concentration of Rb^+ in the brine, the purification solution still has some interfere ions. Table 5 shows the ratio of coexisting ions and Rb^+ in brine and purifying solution, respectively. The ratio data as follow: Li^+/Rb^+ from 0.7 to 0.001, Na^+/Rb^+ from 64.1 to 0.4, Mg^{2+}/Rb^+ from 951.9 to 15.8, K^+/Rb^+ from 248.3 to 10.5 and Cs^+/Rb^+ from 0.02 to 0.01. All the ratios are sharply decreased in the purification solution compared to that of the brine. There are in line with the result of Table 4 and Fig. 12. Therefore, the present result demonstrates KCuFC/SPSG film could be successfully used the separation of Rb^+ from the brine. Further research is underway.

4. Conclusions

In a word, KCuFC/SPSG film was prepared for the selective extraction of Rb^+ from brine. As verified by the relevant characterized analysis, KCuFC nanoparticles were uniformly spread on the SPSG film. The type of adsorption obtained by kinetic modeling was more consistent with chemisorption. The adsorption capacity of 73.7 $mg \cdot g^{-1}$ could be obtained at about pH 7 and 3 h, and 78.6% of the saturated adsorption capacity could be achieved even in 0.5 h. The resulting KCuFC/SPSG film could quickly adsorb Rb^+ with excellent selectivity and regeneration. After 5 cycles of testing, the saturated adsorption capacity of KCuFC/SPSG film has only decreased by 5.6%. Moreover, KCuFC/SPSG was successfully used to the separation of Rb^+ from the simulation brine with recovery rate of 52.5%. Hence, the synthesized KCuFC/SPSG film offers a potential solution for recovering Rb resource from the brine.

CRediT Authorship Contribution Statement

Huanxi Xu: Experiment, Writing and review original draft. **Guan-Ping Jin:** Project administration, Supervision, Resource, Correction. **Pei-Hua Lin** and **Pei-Jun Liu**: Part data. **Ming Fang**: Software. **Xu Zhang:** Methodology. **Hai-Gang Liu**, **Hui-Bin Guo** and **Chao-Xiang Wu**: Resources.

Declaration of Interest

The authors declare no competing financial interest.

Acknowledgements

This work was supported by the Ministry of Science and Technology of China (Science and Technology to Boost Economy 2020 Key Project, SQ2020YFF0412719 and SQ2020YFF0404901). The Key Research and Development and Transformation Program Funding in Qinghai Province (2021-GX-105). Major projects of Anhui Province and Anhui Province Key Research and Development Plan (202104e11020005).

References

[1] J. Jandová, P. Dvořák, J. Formánek, H.N. Vu, Recovery of rubidium and potassium alums from lithium-bearing minerals, *Hydrometallurgy* 119–120 (2012) 73–76.
[2] M. Hosseini, B.M. Sparkes, G. Campbell, P.K. Lam, B.C. Buchler, High efficiency coherent optical memory with warm rubidium vapour, *Nat. Commun.* 2 (2011) 174.
[3] M.H. Al-Mallah, Should patients hold proton pump inhibitors prior to ^{82}Rubidium positron emission tomography myocardial perfusion imaging? *J. Nucl. Cardiol.* 27 (5) (2020) 1452–1455.
[4] A. Fioretti, C. Amiot, C.M. Dion, O. Dulieu, M. Mazzoni, G. Smirne, C. Gabbanini, Cold rubidium molecule formation through photoassociation: A spectroscopic study of the O_g- long-range state of $^{87}Rb_2$, *Eur. Phys. J. D At. Mol. Opt. Plasma Phys.* 15 (2) (2001) 189–198.
[5] A. Baranov, S. Ermak, R. Lozov, V. Semenov, Comparison of gravitational and light frequency shifts in rubidium atomic clock, *Universe* 7 (1) (2020) 3.
[6] I.V. Pekov, N.N. Kononkova, Rubidium mineralization in rare-element granitic pegmatites of the Voron'i tundras, Kola Peninsula, Russia, *Geochem. Int.* 48 (7) (2010) 695–713.
[7] G. Naidu, S. Jeong, M. Abu Hasan Johir, A.G. Fane, J. Kandasamy, S. Vigneswaran, Rubidium extraction from seawater brine by an integrated membrane distillation-selective sorption system, *Water Res.* 123 (2017) 321–331.
[8] J.F. Zhang, L.R. Yang, T.T. Dong, F. Pan, H.F. Xing, H.Z. Liu, Kinetics-controlled separation intensification for cesium and rubidium isolation from salt lake brine, *Ind. Eng. Chem. Res.* 57 (12) (2018) 4399–4406.
[9] P. Xing, C.Y. Wang, Y.Q. Chen, B.Z. Ma, Rubidium extraction from mineral and brine resources: A review, *Hydrometallurgy* 203 (2021) 105644.
[10] Z.W. Lei, X.W. Li, P.W. Huang, H.M. Hu, Z. Li, Q.W. Zhang, Mechanochemical activation of antigorite to provide active magnesium for precipitating cesium from the existences of potassium and sodium, *Appl. Clay Sci.* 168 (2019) 223–229.
[11] P. Xing, G.D. Wang, C.Y. Wang, B.Z. Ma, Y.Q. Chen, Separation of rubidium from potassium in rubidium ore liquor by solvent extraction with *t*-BAMBP, *Miner. Eng.* 121 (2018) 158–163.
[12] T. Nur, P. Loganathan, M.A.H. Johir, J. Kandasamy, S. Vigneswaran, Removing rubidium using potassium cobalt hexacyanoferrate in the membrane adsorption hybrid system, *Sep. Purif. Technol.* 191 (2018) 286–294.
[13] D.F. Huang, H. Zheng, Z.Y. Liu, A.M. Bao, B. Li, Extraction of rubidium and cesium from brine solutions using a room temperature ionic liquid system containing 18-crown-6, *Pol. J. Chem. Technol.* 20 (2) (2018) 40–46.
[14] B.C. Li, H.N. Liu, X.S. Ye, S.Y. Li, Z.J. Wu, Rubidium and cesium ion adsorption by a potassium titanium silicate-calcium alginate composite adsorbent, *Sep. Sci. Technol.* 49 (7) (2014) 1076–1085.
[15] D.H. Ding, Z.Y. Zhang, R.Z. Chen, T.M. Cai, Selective removal of cesium by ammonium molybdophosphate-polyacrylonitrile bead and membrane, *J. Hazard. Mater.* 324 (Pt B) (2017) 753–761.
[16] G. Naidu, P. Loganathan, S. Jeong, M. Abu Hasan Johir, V.H.P. To, J. Kandasamy, S. Vigneswaran, Rubidium extraction using an organic polymer encapsulated potassium copper hexacyanoferrate sorbent, *Chem. Eng. J.* 306 (2016) 31–42.
[17] C.Y. Jiang, J.H. Ni, G.P. Jin, Magnetic potassium cobalt hexacyanoferrate nanocomposites for efficient adsorption of rubidium in solution, *Sep. Purif. Technol.* 296 (2022) 121383.
[18] J.Y. Yang, X.G. Luo, T.S. Yan, X.Y. Lin, Recovery of cesium from saline lake brine with potassium cobalt hexacyanoferrate-modified chrome-tanned leather scrap adsorbent, *Colloids Surf. A* 537 (2018) 268–280.
[19] R.Y. Wang, B. Shyam, K.H. Stone, J.N. Weker, M. Pasta, H.W. Lee, M.F. Toney, Y. Cui, Reversible multivalent (monovalent, divalent, trivalent) ion insertion in open framework materials, *Adv. Energy Mater.* 5 (12) (2015) 1401869.
[20] Z.D. Wang, S.J. Guo, Z.J. Wu, H.L. Fan, G.Q. Guan, X.G. Hao, A smart potential-responsive ion exchange nanomaterial with superparamagnetism for cesium ion separation and recovery, *Sep. Purif. Technol.* 187 (2017) 199–206.
[21] C. Vincent, A. Hertz, T. Vincent, Y. Barré, E. Guibal, Immobilization of inorganic ion-exchanger into biopolymer foams – Application to cesium sorption, *Chem. Eng. J.* 236 (2014) 202–211.
[22] G. Naidu, T. Nur, P. Loganathan, J. Kandasamy, S. Vigneswaran, Selective sorption of rubidium by potassium cobalt hexacyanoferrate, *Sep. Purif. Technol.* 163 (2016) 238–246.
[23] S.Y. Ding, L.L. Zhang, Y. Li, L.A. Hou, Engineering a high-selectivity PVDF hollow-fiber membrane for cesium removal, *Engineering* 5 (5) (2019) 865–871.
[24] C. Yu, J. Lu, Z.Q. Hou, Z.F. Ma, X.Y. Lin, Z.Q. Dong, W.D. Xing, Y.S. Yan, Y.L. Wu, Mixed matrix membranes for rubidium-dependent recognition and separation: A synergistic recombination design based on electrostatic interactions, *Sep. Purif. Technol.* 255 (2021) 117727.
[25] H. Wang, H. Li, L. Yu, Y. Jiang, W. K Wang, Synthesis of porous Al_2O_3-PVDF composite separators and their application in lithium-ion batteries, *J. Appl. Polym. Sci.* 130 (4) (2013) 2886–2890.
[26] X.R. Meng, Y.R. Tian, M.Y. Tang, R.K. Qiao, Separation and enrichment of Rb(I) in dicyclohexano 18 crown 6($DCH_{18}C_6$)/PVC polymer inclusion membrane assisted by electric field, *J. Environ. Chem. Eng.* 9 (6) (2021) 106712.
[27] J.T. He, L.Y. Mao, X.H. Ma, J.Y. Hua, Z.Y. Cui, B.Q. He, H.C. Pei, J.X. Li, Highly-efficient adsorptive separation of Cs^+ from aqueous solutions by porous polyimide membrane containing dibenzo-18-crown-6, *Sep. Purif. Technol.* 299 (2022) 121757.
[28] X.D. Zheng, Y.Y. Wang, F.X. Qiu, Z.Y. Li, Y.S. Yan, Dual-functional mesoporous films templated by cellulose nanocrystals for the selective adsorption of lithium and rubidium, *J. Chem. Eng. Data* 64 (3) (2019) 926–933.
[29] A. Ozden, M. Ercelik, Y. Devrim, C.O. Colpan, F. Hamdullahpur, Evaluation of sulfonated polysulfone/zirconium hydrogen phosphate composite membranes for direct methanol fuel cells, *Electrochim. Acta* 256 (2017) 196–210.
[30] Y. Devrim, S. Erkan, N. Baç, I. Eroğlu, Preparation and characterization of sulfonated polysulfone/titanium dioxide composite membranes for proton exchange membrane fuel cells, *Int. J. Hydrog. Energy* 34 (8) (2009) 3467–3475.
[31] P. Lu, Y. Wang, L. Wang, Y.Y. Wei, W.J. Li, Y.S. Li, C.Y. Tang, Immobilization of sulfonated polysulfone *via* 2D LDH nanosheets during phase-inversion: A novel strategy towards greener membrane synthesis and enhanced desalination performance, *J. Membr. Sci.* 614 (2020) 118508.
[32] X.F. Sun, Y. Wang, H.Y. Zhang, Y. Shen, Q.A. Shi, H.H. Chen, J.K. Sun, Z.G. Zhang, Fabrication and performance of the ammonium molybdophosphate/polysulfone mixed matrix membranes for rubidium adsorption in aqueous solution, *J. Appl. Polym. Sci.* 139 (11) (2022) 51798.

[33] Y. Vasseghian, E.N. Dragoi, F. Almomani, V.T. Le, M. Berkani, Graphene-based membrane techniques for heavy metal removal: A critical review, *Environ. Technol. Innov.* 24 (2021) 101863.
[34] W.J. Peng, H.Q. Li, Y.Y. Liu, S.X. Song, A review on heavy metal ions adsorption from water by graphene oxide and its composites, *J. Mol. Liq.* 230 (2017) 496–504.
[35] Y. Kim, Y.K. Kim, S. Kim, D. Harbottle, J.W. Lee, Nanostructured potassium copper hexacyanoferrate-cellulose hydrogel for selective and rapid cesium adsorption, *Chem. Eng. J.* 313 (2017) 1042–1050.
[36] Y. Nagaoka, S. Adachi, Photoluminescent properties of NaCl: Ce^{3+} phosphor synthesized using antisolvent crystallization, *J. Lumin.* 145 (2014) 797–802.
[37] M.B. Nguyen, G.H. Le, T.T. Pham, G.T.T. Pham, Q.V. Tran, N.T. Nguyen, V. Thi Thu Ha, T.V. Nguyen, T.A. Vu, High CO performance of graphene oxide modified with CuCl by using "ion implantation" method, *Mater. Res. Express* 7 (10) (2020) 105008.
[38] X.Y. Tang, S.Y. Wang, Z.H. Zhang, Z.J. Li, L. Wang, L.Y. Yuan, B.R. Wang, J. Sun, L. R. Zheng, H.Q. Wang, W.Q. Shi, Graphene oxide/chitosan/potassium copper hexacyanoferrate (II) composite aerogel for efficient removal of cesium, *Chem. Eng. J.* 444 (2022) 136397.
[39] M. Fang, W.F. Chu, J.S. Cui, G.P. Jin, C.Q. Tian, Adsorption application of Rb^{+} on hydrogels of hydroxypropyl cellulose/polyvinyl alcohol/reduced graphene oxide encapsulating potassium cobalt hexacyanoferrate, *Appl. Organomet. Chem.* 36 (10) (2022) e6827.